
Article:
Asiagbe, K.S., Fairweather, M., Njobuenwu, D.O. et al. (1 more author) (2019) Large eddy simulation of microbubble dispersion and flow field modulation in vertical channel flows. AIChE Journal, 65 (4). pp. 1325-1339. ISSN 0001-1541

https://doi.org/10.1002/aic.16509

Large Eddy Simulation of Microbubble Dispersion and Flow Field Modulation in Vertical Channel Flows

Kenneth S. Asiagbe, Michael Fairweather, Derrick O. Njobuenwu, Marco Colombo[1]

School of Chemical and Process Engineering, University of Leeds, Leeds LS2 9JT, UK

Abstract

Turbulent liquid-gas vertical channel flows laden with microbubbles are investigated using large eddy simulation (LES) two-way coupled to a Lagrangian bubble tracking technique. Upward and downward flows at shear Reynolds numbers of $Re_\tau = 150$ and 590 are analysed for three different microbubble diameters of 110 μm, 220 μm and 330 μm. Predicted results are compared with published direct numerical simulation results although, with respect to comparable studies available in the literature, the range of bubble diameters and shear Reynolds numbers considered herein is extended to larger values. Microbubble concentration profiles are analysed, with the microbubbles segregating at the wall in upflow conditions and moving towards the channel centre in downflow. The various forces acting on the bubbles, and the effect of the flow turbulence on the bubble concentration, are considered and quantified. Overall, the results suggest that the level of detail achievable with LES is sufficient to predict the fluid structures impacting bubble behaviour. Therefore, LES coupled with Lagrangian bubble tracking shows promise for enabling the reliable prediction of bubble-laden flows that are of industrial relevance.

Keywords

Eulerian-Lagrangian, large eddy simulation, microbubbles, turbulence modulation, vertical channel flows

Introduction

Bubbly flows, where gaseous bubbles are dispersed in a continuous liquid flow, are widely encountered in many industrial and natural processes. Bubbly flows with engineering applications include the transfer and processing of oil and gas[1], cooling devices in nuclear reactors and steam generators[2] bubble column reactors, and the evaporation and condensation of refrigerants in air conditioning equipment, to name but a few. Natural occurrences of bubbly flows can be found, for example, in the mass transfer between the oceans and the atmosphere[3-

[1] Corresponding Author. E-mail: M.Colombo@leeds.ac.uk; Tel: +44 (0) 113 343 2351

[5]. In engineering applications, such flows need to be predicted with accuracy and reliability in order to successfully design, optimise and maintain systems that incorporate, and rely on, bubbly flows[6].

Bubbly flows are highly complex as it is necessary to understand the effect of the continuous phase on the bubbles' spatial and velocity distributions. In turn, the presence of the bubbles affects the continuous liquid flow and pressure drop in any system, particularly in the near-wall region[7]. Understanding and accurately predicting these behaviours is therefore problematic, particularly given that the flow is sensitive to the number of bubbles present, including their size and shape, and to the fluid and bubble velocities. It is also further complicated in many flows by the occurrence of bubble-bubble collisions, and bubble coalescence and break-up, and the local and instantaneous, and frequently evolving, distribution of bubble sizes. The behaviour of bubbly flows has also been demonstrated to depend on many other factors, including the flow direction of the liquid[8].

Physical and numerical modelling of bubbly flows has been performed extensively[9-11], although experimental work has generally been limited to the measurement of bubble and liquid velocity fields, and bubble size distribution. Although these measurements are useful and of value both in increasing our understanding of such flows and in providing data for the validation of numerical models, they generally require large length scale test rigs and high-resolution measurement techniques to provide accurate data, with associated high costs. It is also challenging to track in detail the behaviour of individual bubbles in such experiments. Numerical modelling, therefore, has a complementary role in understanding the dynamics of bubbly flows. Normally, the carrier fluid is treated as the continuous phase, with the bubbles considered as the dispersed or discrete phase, with Eulerian-Eulerian[12,13], Eulerian-Lagrangian[14-16], and fully-resolved[17] approaches adopted. Discussions of the relative merits and disadvantages of each of these approaches are available elsewhere[18-20]. In this work, an Eulerian-Lagrangian approach based on large eddy simulation (LES) is adopted as it provides useful and detailed insights into both the fluid and bubble behaviour, whilst having significantly lower computational costs than a fully-resolved approach.

In recent years, bubbly flows have been the subject of numerous investigations[14,15,21,22]. A number of these, such as the experiments presented by Hosokawa et al.[23] and the numerical simulations of Ervin and Tryggvason[24] and Pang et al.[25], focused on the dispersion of bubbles and their complex interactions with the turbulent flow structures. Pang et al.[26] investigation of a channel flow demonstrated that the liquid phase turbulence is intensified near the walls and slightly weakened in the central region due to bubble addition. Giusti et al.[14] used one-way

coupled numerical simulations to study the effect of the lift force on the behaviour of non-deformable microbubbles dispersed in a turbulent vertical channel flow. Delnoij et al.[27] and Lain et al.[28] investigated the enhanced turbulent mixing of dispersed reagents promoted by buoyant bubbles in devices such as bubble columns. Santarelli and Fröhlich[29] also applied direct numerical simulation (DNS) and the immersed boundary method to a dilute and a denser swarm of bubbles rising in a vertical channel flow configuration. This work investigated the interaction between bubbles and the fluid phase and provided instantaneous visualizations of the flow and a detailed analysis of single-point statistics, two-point correlation functions and pair correlation functions for both phases.

Wall-bounded bubbly flows exhibit interesting bubble dynamics. During flow against the direction of gravity (upflow), the bubbles move faster than the liquid and, as long as their shape remains close to spherical, they are pushed towards the wall by the lift force. In regions very close to the wall, the flow of liquid between the bubbles and the wall generates a wall lubrication force that tends to prevent the bubbles from touching the wall. Conversely, for flows with the direction of gravity (downflow), the bubbles move slower than the liquid and are pushed by the lift force towards the centre of the flow. Both of these two phenomena have been experimentally observed[9-11]. In addition, when the diameter of the bubbles increases above a certain value, deformation of the bubbles by the inertia of the surrounding liquid can alter the fluid circulation around them, changing the sign of the lift force that consequently starts to push the bubbles, in upflow conditions, towards the centre of the flow[24]. Complementing previous knowledge, an extensive study of the mutual interactions between microbubbles and turbulence in a vertical channel flow, performed using an Eulerian-Lagrangian approach based on direct numerical simulation, was undertaken by Molin et al.[15]. Four diameters of microbubble were subjected to gravity, drag, added mass, pressure gradient, Basset history and lift forces. The authors observed different bubble distributions in the two flow configurations considered, with lift segregating bubbles at the wall in upflow and preventing bubbles from reaching the near-wall region in downflow conditions. In addition, they observed significant increases, and decreases, of both the wall shear and liquid flow rate in upflow, and downflow, respectively, due to local momentum exchange with the carrier fluid and to the differences in the bubble distribution.

Although DNS resolves all the scales of a flow[14,25,29], and provides results comparable to those available from experimental studies, its computational cost means that it is still restricted to the simulation of relatively few bubbles, particularly when coupled with interface tracking techniques to resolve bubble motion, and low Reynolds number flows. Even when coupled to

a Lagrangian methodology that allowed the tracking of significant numbers of bubbles (~ several hundred thousand), DNS studies in closed ducts have been mostly limited to 150 – 200 shear Reynolds number flows[14,15,21,26]. Instead LES, where the large scales of turbulent motion are resolved while the subgrid turbulent scales and their effect on the mean flow are modelled, allows complex flows with industrial relevance to be predicted more readily. In a liquid-gas turbulent flow, the large-scale turbulent structures interact with the bubbles and are responsible for the macroscopic bubble motion, whilst small-scale turbulent structures only τcaptured in LES, and the less energetic small scales are approximated using a subgrid-scale (SGS) model, coupling of bubble tracking technique and LES can in principle reproduce the large scale motion responsible for the bubble motion. In our previous works, an LES Eulerian-Lagrangian model was successfully applied to horizontal channel flows[16,30] and its initial application to a vertical channel flow was investigated[31]. In these studies, LES was demonstrated to achieve a level of detail sufficient to predict bubbly flows with accuracy. Moreover, because of the less demanding computational requirements, LES was applied to significantly higher Reynolds number with respect to comparable DNS studies, closer to the bubbly flows of relevance in industry.

In this work, the LES Eulerian-Lagrangian model is applied to the study the flow of air microbubbles in water in vertical upward and downward channel flows. A full-validation of the model is provided, starting from the single-phase flow and subsequently comparing predictions with the bubbly flow DNS-based results of Molin et al.[15] at a shear Reynolds number $Re_\tau = 150$. With respect to our previous work[31], the range of microbubble diameters is extended to $d_b = 330$ μm to provide additional details with respect to the complex mutual interactions between turbulence and the bubbles at various bubble sizes, particularly near the channel walls. Extension of the modelling approach to the higher Reynolds number $Re_\tau = 590$ was initially demonstrated elsewhere[31]. Here, the effect of higher levels of turbulence on the bubble distribution and the modifications, induced by the presence of these bubbles, to the continuous phase flow field are investigated in detail. It is demonstrated how at this higher Reynolds number, due to the enhanced turbulent dispersion, the preferential concentration of bubbles diminishes and lift is no longer the dominant mechanism that drives the bubble lateral distribution. These results, as well as providing meaningful insight into the mechanisms of interfacial momentum transfer, are also of value in support of the development of improved closures for macroscopic averaged models, such as Eulerian-Eulerian two-fluid methodologies.

Mathematical Modelling

Large eddy simulation

The LES equations can be obtained by applying a spatial filter to the equations of motion. The filtered continuity and momentum equations are then given as:

$$\frac{\partial \bar{u}_i}{\partial x_i} = 0, \tag{1}$$

$$\frac{\partial \bar{u}_i}{\partial t} + \bar{u}_j \frac{\partial \bar{u}_i}{\partial x_j} = -\frac{1}{\rho}\frac{\partial \bar{p}}{\partial x_i} - \frac{\partial}{\partial x_j}\left(\bar{\sigma}_{ij} + \tau_{ij}\right) + \frac{\overline{\Delta \mathrm{p}}}{\rho L_z}\delta_{i3} + \frac{f_{2w,i}}{\rho}. \tag{2}$$

The overbar identifies filtered quantities, ρ represents the fluid density, u is the fluid velocity and p is the pressure. The last two terms on the right hand side (RHS) of Eq. (2) represent the mean pressure gradient, $\overline{\Delta p}/L_z$, required to drive the flow and the action on the fluid of the bubbles, $f_{2w,i}$, given by the summation of all the hydrodynamic forces acting on the bubbles apart from gravity and buoyancy. The mean pressure gradient, taking into account gravity and buoyancy forces, is given as[32]:

$$\frac{\overline{\Delta p}}{L_z} = -\frac{\rho u_\tau^2}{h} \pm \alpha_b(\rho_l - \rho_b)g, \tag{3}$$

where u_τ is the fluid shear velocity, α_b is the bubble volume fraction, h is the channel half-height, ρ_b is the bubble density, g is acceleration due to gravity and the $\pm$ depends on the direction of gravity.

In Eq. (2), σ_{ij} is the viscous stress, given by:

$$\bar{\sigma}_{ij} = -2\nu\bar{S}_{ij} = -\nu\left(\frac{\partial \bar{u}_i}{\partial x_j} + \frac{\partial \bar{u}_j}{\partial x_i}\right), \tag{4}$$

where ν is the fluid kinematic viscosity and S_{ij} is the strain-rate tensor. τ_{ij} in Eq. (2) is the SGS stress tensor arising from the filtering operation:

$$\tau_{ij} = \overline{u_i u_j} - \tilde{\bar{u}}_i \tilde{\bar{u}}_j. \tag{5}$$

This term is required to close the system of equations and it is approximated by the product of an SGS turbulent kinematic viscosity, ν_{sgs}, and the resolved part of the strain-rate tensor. The

SGS kinematic viscosity is taken as the product of the filter width Δ and an appropriate velocity scale:

$$\nu_{sgs} = (C\bar{\Delta})^2 \|\bar{S}\|, \tag{6}$$

where $||\bar{S}|| = \sqrt{2\bar{S}_{ij}\bar{S}_{ij}}$. The anisotropic part of the SGS stress tensor is given by:

$$\tau_{ij}^{a} = -2(C\bar{\Delta})^2 \|\bar{S}\|\bar{S}_{ij}. \tag{7}$$

The SGS kinematic viscosity is calculated from the dynamic Smagorinsky model[33,34], in which the model coefficient C is dynamically determined by applying a second filter, usually called the test filter. The test filtered SGS stresses result:

$$T_{ij} = \widetilde{\overline{u_i}\overline{u_j}} - \tilde{\bar{u}}_i\tilde{\bar{u}}_j. \tag{8}$$

In this equation, the tilde represents the test filter operation. The parameters T_{ij} and $\tilde{\tau}_{ij}$ are unknown, but are related by Germano's identity[33] through the small resolved scales:

$$L_{ij} = T_{ij} - \tilde{\tau}_{ij} = \widetilde{\overline{u_i}\overline{u_j}} - \tilde{\bar{u}}_i\tilde{\bar{u}}_j. \tag{9}$$

To derive the required expression for *C*, some form of relationship between the model constant values C and $C^2(\tilde{\bullet})$ at the grid- and test-filter levels must be specified and, based on the hypothesis that the cut-off length falls inside the inertial sub-range, $C^2 = C^2(\tilde{\bullet})^2$. However, such a sub-range is not guaranteed to occur in wall bounded or low Reynolds number flows, with the largest deviation from universality of the SGS motions expected to occur in the regions of weakest resolved strain. Based on this, the two values of the model parameter at two different filter levels are liable to differ. To account for this, di Mare and Jones[35] proposed the following:

$$C^2(\tilde{\bullet}) = C^2\left(1 + \frac{\varepsilon}{2\sqrt{2\widetilde{\Delta^2}}\ \|\ \tilde{\bar{s}}\ \|\|\ \tilde{\bar{s}}^a\ \|^2}\right), \tag{10}$$

where ε is the assumed turbulence energy dissipation rate, such that $\varepsilon \approx v^3/l;\ v$ and l are the velocity and length scales, respectively.

Eq. (10) is based on the assumption that the scale invariance of C can only be invoked if the cut-off falls inside an inertial sub-range, and when this occurs, the modelled dissipation should represent the entire dissipation in the flow. Conversely, in the high Reynolds number limit, the dissipation is only determined by v and l so that the ratio of ε to $\widetilde{\Delta}^2\left\|\tilde{S}\right\|^3$ measures how far the flow is from scale preserving conditions. Eq. (10) represents a first-order expansion of other scale dependent expressions for C, e.g. that of Porté-Agel et al.[36], which also uses a single length and velocity scale. Equations (9) and (10) with contraction of both sides with the tensor $\tilde{\bar{s}}$ then give:

$$C^2 = \frac{\left[2\sqrt{2(C_*^2\Delta)^2}\parallel \bar{s} \parallel\parallel \tilde{\bar{s}}_{ij}^a \parallel \tilde{\bar{s}}_{ij}^a - L_{ij}^a \tilde{\bar{s}}_{ij}^a\right]}{\varepsilon + 2\sqrt{2\widetilde{\Delta}^2}\parallel \tilde{\bar{s}} \parallel\parallel \tilde{\bar{s}}^a \parallel^2}, \tag{11}$$

where C_*^2 is a provisional value for the field C^2, e.g. its value at the previous time step[34]. The dependence embodied in Eq. (11) gives a simple correlation for C^2. The main advantage of this method is that it is well-conditioned and avoids the spiky and irregular behaviour exhibited by some implementations of the dynamic model and, as the resolved strain tends to zero, C^2 also tends to zero, while $C^2(\tilde{\bullet})^2$ remains bounded. The dissipation term also yields smooth C^2 fields without a need for averaging, and the maxima of C^2 are of the same order of magnitude as Lilly[37] estimates for the Smagorinsky model constant. Negative values of the model parameters are not prevented, with such values set to zero to prevent instability. Negative values of the SGS viscosity are similarly set to zero. Test filtering was performed in all space directions, with no averaging of the calculated model parameter field. The ratio $\widetilde{\Delta}/\Delta$ was set to 2 and the filter width determined from $\Delta = \left(\Delta_x\Delta_y\Delta_z\right)^{1/3}$, where Δ_x, Δ_y, and Δ_z denote the physical grid spacing in the three coordinate directions.

Lagrangian tracking of bubble motion

Bubble motion in a turbulent flow field is obtained by solving Newton's second law for each individual bubble[38]. The density of the microbubbles is much lower than the density of the carrier fluid resulting in a density ratio $\rho_b/\rho_l = 1.3 \text{ x } 10^{-3}$. The microbubbles are subjected to drag, lift, gravity, buoyancy, pressure gradient and added mass forces, and a stochastic

contribution arising from SGS velocity fluctuations. The Basset history force is negligible in comparison with the other forces and has been neglected[39,40]. Therefore, the motion of microbubbles obeys the following Lagrangian equation written per unit mass:

$$\frac{\mathrm{d}\mathbf{v}}{\mathrm{d}t} = \left(1 - \frac{\rho_l}{\rho_b}\right) g + \frac{\mathbf{u} - \mathbf{v}}{\tau_b} C_{SN} + C_L \frac{\rho_l}{\rho_b} [(\mathbf{u} - \mathbf{v}) \times \boldsymbol{\omega}] + \frac{\rho_l}{\rho_b} \frac{\mathrm{d}\mathbf{u}}{\mathrm{d}t} + \frac{\rho_l}{2\rho_b} \left(\frac{\mathrm{d}\mathbf{u}}{\mathrm{d}t} - \frac{\mathrm{d}\mathbf{v}}{\mathrm{d}t}\right) + \boldsymbol{\chi_{sgs}}. \quad (12)$$

The terms on the right-hand side of Eq. (12) represent the gravity-buoyancy, drag, shear-lift, pressure gradient and added mass forces per unit mass, respectively, while the last term $\boldsymbol{\chi_{sgs}}$ represents the effect of SGS velocity fluctuations on the bubble motion. Subscripts l and b represent the liquid and bubbles, respectively. $\boldsymbol{\omega} = 0.5 \times \nabla \mathbf{u}$ is the fluid vorticity and τ_b is the bubble relaxation time, corrected to account for added mass effects to give $\check{\tau}_b = \tau_b(1 + \rho_l/2\rho_b)$. The bubble position vector $\mathbf{x}_b$ can be obtained by further differentiation of Eq. (12). The coefficient C_{SN} represents the non-linear[41] drag coefficient written, with respect to the bubble Reynolds number $Re_b = |\mathbf{u} - \mathbf{v}| d_b/\nu$, as:

$$C_{SN} = (1 + 0.15 Re_b^{0.687}). \quad (13)$$

The lift coefficient C_L is also a function of Re_b and the dimensionless shear rate Sr_b and it is computed from the correlation of Legendre and Magnaudet[42]:

$$C_L = \sqrt{\left(C_L^{lowRe}\right)^2 + \left(C_L^{highRe}\right)^2}, \quad (14)$$

$$C_L^{lowRe} = \frac{6}{\pi^2} (Re_b Sr_b)^{-0.5} \left[\frac{2.255}{(1 + 0.2\xi^{-2})^{1.5}}\right], \quad (15)$$

$$C_L^{highRe} = \frac{1}{2}\left(\frac{1 + 16/Re_b}{1 + 29/Re_b}\right), \quad (16)$$

with $Sr_b = |\boldsymbol{\omega}| d_b/(2|\mathbf{u} - \mathbf{v}|)$ and $\xi = \sqrt{Sr_b/Re_b}$.

The last term in Eq. (12) is determined using a stochastic Markov model[43] in order to represent the influence of unresolved SGS velocity fluctuations on bubble acceleration, and is evaluated from:

$$\boldsymbol{\chi_{sgs}} = C_0 \left(\frac{k_{sgs}}{\tau_t}\right) \mathrm{d}\mathbf{W}_t/\mathrm{d}t, \quad (17)$$

where k_{sgs} is the unresolved kinetic energy of the liquid phase, C_0 is a model constant taken as unity and $\mathrm{d}\mathbf{W}_t$ represents the increment of the Wiener process. During the simulation, $\mathrm{d}\mathbf{W}_t$ is represented by $\xi_i \times \sqrt{\Delta t}$, where ξ_i is a random variable sampled from a normal distribution with zero mean and a variance of unity, and which is independent for each time step and for each velocity component. τ_t is a sub-grid time scale which affects the rate of interaction between the bubble and turbulence dynamics, defined as:

$$\tau_t = \frac{\tau_b^{1.6}}{\left(\Delta/k_{sgs}^{0.5}\right)^{0.6}}. \tag{18}$$

The SGS kinetic energy is obtained from $k_{sgs} = \left(2\Delta\nu_{sgs}\bar{S}_{ij}\bar{S}_{ij}\right)^{2/3}$, an expression derived using equilibrium arguments[43].

Two-way coupling effects

When the bubble volume fraction α_b in a flow becomes greater than 10^{-6}, the momentum transfer from the bubble suspension is large enough to modify the structure of the turbulence in the continuous phase and the flow is referred to as two-way coupled[44]. The coupling effect is enforced by the addition of the source term $f_{2w,i}$, which represents the force per unit volume exerted by the bubbles on the fluid, in the fluid momentum balance (Eq.(2)):

$$f_{2w,i} = \frac{1}{\Delta^3}\sum_{j=1}^{n_b} f_{H,i}^{j}, \tag{19}$$

where the summation is defined over the number of bubbles n_b in the finite-volume cell under consideration, $f_{H,i}^{j}$ is the source term arising from the j^{th} bubble in the i^{th} direction and the subscript H represents the hydrodynamic force terms. In Eq. (19), the force contribution is scaled with the volume of the cell. In view of the number of bubbles employed (181,272 maximum), the number of cells (more than 2 million) used ensures a high resolution of the two-way coupling field, with only a few bubbles simultaneously present in the same cell. Therefore, no significant dependencies of the two-way coupling term on the mesh are expected. In the present case, the relevant source term used in the momentum equation is the summation of all the hydrodynamic forces (drag, shear-lift, pressure gradient and added mass), with the body forces (gravity and buoyancy) included in the pressure gradient term:

$$f_{H,i}^{j} = -m_b \left[\frac{\mathrm{d}v_i}{\mathrm{d}t} - \left(1 - \frac{\rho_l}{\rho_b}\right) g_i\right], \tag{20}$$

where m_b is the mass of a bubble and g is gravitational acceleration, with $g = -9.81$ and $g = 9.81$ m s^{-2} for upflow and downflow, respectively.

Table 1: Non-dimensional wall shear stress, shear velocity and Reynolds number for the single-phase and the two-way coupled simulations at nominal shear Reynolds of 150 and 590.

Unladen flow	Two-way coupled flow	
	Upflow	Downflow
$Re_\tau = 150$	$Re_\tau = 172$	$Re_\tau = 122$
$\tau_w^+ = 1$	$\tau_w^+ = 1.31$	$\tau_w^+ = 0.66$
$u_\tau = 7.5 \times 10^{-3}\mathrm{ms}^{-1}$	$u_\tau = 8.58 \times 10^{-3}\mathrm{ms}^{-1}$	$u_\tau = 6.11 \times 10^{-3}\mathrm{ms}^{-1}$
Unladen flow	Upflow	Downflow
$Re_\tau = 590$	$Re_\tau = 612$	$Re_\tau = 562$
$\tau_w^+ = 1.00$	$\tau_w^+ = 1.07$	$\tau_w^+ = 0.91$
$u_\tau = 2.95 \times 10^{-2}\mathrm{ms}^{-1}$	$u_\tau = 3.06 \times 10^{-2}\mathrm{ms}^{-1}$	$u_\tau = 2.81 \times 10^{-2}\mathrm{ms}^{-1}$

As already shown in Eq. (3), to account for the effect of microbubbles on the fluid, the pressure gradient is modified from the single-phase flow definition with an additional pressure difference induced by the presence of the microbubbles. In other words, the sum of gravitational and frictional pressure losses is kept constant. Therefore, in upflow, the presence of the lighter mixture allows the fluid to flow faster. In a similar way, in downflow, the flow is slower because of the reduced gravitational pressure gain induced by the lighter mixture. This suggests the introduction of new definitions for the shear velocity and the shear Reynolds number for upflow and downflow ($u_\tau = (\tau_w/\rho_l)^{1/2}$ and $Re_\tau = u_\tau h/\nu$), where the value of the wall shear stress is obtained from $\tau_{w,2w} = \left[\frac{\Delta P}{L_z} \pm \alpha(\rho_l - \rho_b)g\right]\frac{L_x}{2}$[15]. In this work two shear Reynolds numbers, Re_τ = 150 and 590, were investigated, and the single-phase and two-way coupled values of the wall shear stress, shear velocity and Reynolds number for these cases are summarized in Table 1.

Numerical Solution

The computational domain employed was a channel bounded by two infinite flat parallel walls, as illustrated in Fig. 1, with the *x, y*, and *z* axes pointing in the wall-normal, spanwise and streamwise directions, respectively. The dimensions of the computational domain were set to $L_x \times L_y \times L_z = 2h \times 2\pi h \times 4\pi h$ and discretised using $N_x \times N_y \times N_z = 129 \times 128 \times 128$ grid points. The grid nodes were uniformly distributed along the y and z axes, and non-uniformly using a hyperbolic function[45] in the wall-normal direction. The no-slip boundary condition was imposed at the channel walls and periodic boundary conditions were imposed in the streamwise and spanwise directions, with the flow being driven by the imposed streamwise fixed pressure gradient. The BOFFIN (Boundary Fitted Flow Integrator) code[43] was used to solve the governing flow equations. This uses a second-order-accurate finite-volume method, based on an implicit low-Mach-number pressure-based formulation with a co-located storage arrangement and pressure smoothing according to the approach of Rhie and Chow[46]. For the momentum equation convection terms an energy-conserving discretisation scheme is used, and all other spatial derivatives are approximated by second-order central differences. For time discretization, a fully implicit scheme is employed with a two-step second-order time accurate approximate factorization method to ensure mass conservation. The code has been applied extensively in the LES of reacting[47,48] and non-reacting turbulent flows[43,49]. For further details of the numerical methods used in BOFFIN, readers are referred to those publications and relevant references therein.

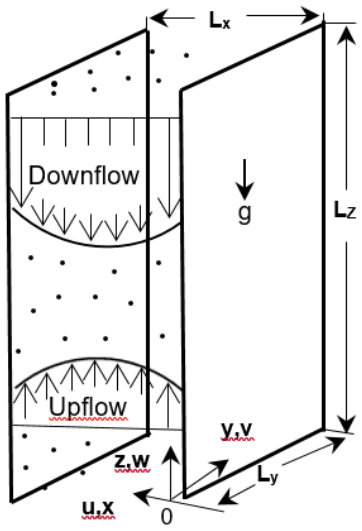

Figure 1: Coordinate system and channel geometry.

Air bubbles with a density ρ_b = 1.3 kg m^{-3} were uniformly introduced into fully-converged single-phase flow solutions at shear Reynolds numbers Re_τ = 150 and 590, with the initial velocity of the bubbles equal to the fluid velocity at the bubble location, obtained by interpolation. Water was used as the continuous phase, with a kinematic viscosity ν = 10^{-6} m^{2}s^{-1} and a density ρ_l = 1000 kg m^{-3}. Three bubble sizes, with diameters d_b = 110, 220 and 330 μm, were selected, and the bubble volume fraction was chosen as $\alpha_b = 1.0 \times 10^{-4}$, high enough for the microbubbles to affect the continuous fluid flow field but, at the same time, low enough to ensure negligible bubble-bubble interactions. This corresponds to a total number of 181,272 microbubbles for the d_b= 110 μm case, 22,700 for d_b= 220 μm and 6,714 for d_b= 330 μm. Simulations were made for both upward and downward vertical channel flows.

The flow direction of individual microbubbles was obtained from integration of the Lagrangian tracking equation, Eq. (12), using a fourth-order Runge-Kutta scheme. Perfectly elastic collisions were assumed at the wall when the microbubble centre was at a distance from the wall equal to the bubble radius. Even though this is a simplistic assumption for bubbles, which may deform when approaching and hitting a wall, a reliable and robust modelling framework for such interactions is not yet available. Therefore, the simple hard sphere collision assumption has been adopted. The time-step for the bubble tracker was chosen to be equal to the fluid flow solver time-step, this corresponding to roughly one-quarter of the bubble response time ($\tau_b = \rho_b d_b^2/18\mu$) for both Reynolds numbers considered. The total simulation time, expressed in wall units and determined from $t^+ = tu_\tau^2/\upsilon$ (where t is the computational time in seconds), was 1500 for the upflow and 2000 for the downflow cases at $Re_\tau = 150$, and 1200 for the upflow and 1400 for the downflow cases at $Re_\tau = 590$, with averaging carried out after 1000 t^+. Further details of relevant liquid and bubble parameters used in the simulations are given in Table 2.

Table 2: Fluid and bubble computational parameters for the two flow Reynolds numbers considered.

Re_τ = 150		Re_b = 2272		u_τ(ms^{-1}) = 7.5 × 10^{-3}	u_{bulk} = 0.114	
$d_b(\mu m)$	d_b^+	$\tau_b(\mu s)$	τ_b^+	$\tilde{\tau}_b(s)$	$\tilde{\tau}_b^+$	n_b
110	0.83	0.87	4.89 × 10^{-5}	3.37 × 10^{-4}	0.02	181,272
220	1.65	3.50	1.97 × 10^{-4}	1.35 × 10^{-3}	0.07	25,400
330	2.48	7.87	4.42 × 10^{-4}	3.03 × 10^{-3}	0.17	6,714

Re_τ = 590		Re_b = 11033		u_τ = 2.95 x 10^{-2}		u_{bulk} = 0.552
d_b (μm)	d_b^+	τ_b(μs)	τ_b^+	$\tilde{\tau}_b(s)$	$\tilde{\tau}_b^+$	n_b
110	3.25	0.87	7.61×10^{-4}	3.37×10^{-4}	0.29	181,272
220	6.49	3.50	3.04×10^{-3}	1.35×10^{-3}	1.17	25,400
330	9.74	7.87	6.84×10^{-3}	3.03×10^{-3}	2.64	6,714

Results and Discussions

In this section, simulation results are discussed, with particular emphasis on the velocity fields of both the fluid and the microbubbles, as well as the microbubble concentration profile. First, the single-phase LES predictions are validated against DNS results for the $Re_\tau = 150$[50] and the $Re_\tau = 590$[51] flows. Bubbly flows in both upflow and downflow are then validated, in part, against the predictions of Molin et al.[15] for bubble sizes d_b = 110 and 220 μm. Simulations are then extended to the cases of d_b = 330 μm and $Re_\tau = 590$, for which no predictions are currently available in the literature. Finally, the role and importance of the different forces acting on the bubbles in the wall-normal direction, and their effect on bubble concentration profiles, are considered.

Single-phase flow

Figure 2 shows the mean streamwise velocity and the root mean square (r.m.s.) of the velocity fluctuations for the single-phase flows at shear Reynolds numbers of 150 and 590. At $Re_\tau = 150$, the LES results are compared against the DNS of Marchioli et al.[50] at the same shear Reynolds number. As shown, both the mean streamwise velocity and the turbulent normal stresses are in good agreement with the DNS predictions, although there is some underestimation in the peak normal stresses in the spanwise and wall-normal directions, and in all normal stress values close to the centre of the flow. For the $Re_\tau = 590$ case, the LES predictions remain in acceptable agreement with the DNS results, even if these are again slightly under-predicted near the wall in the spanwise and wall-normal directions, and near the centre of the channel, particularly in the streamwise direction. The grid resolution used by Moser et al.[51] in their DNS was 384×257×384, whereas for the LES a grid resolution of 129×128×128, as used for the 150 shear Reynolds number case, was maintained, with the latter comparing with a maximum resolution of 192×192×192 used in the DNS computations[50].

Therefore, the LES may be considered relatively highly resolved at $Re_\tau = 150$, compared to the DNS used for comparison purposes, whilst at $Re_\tau = 590$ this is less the case. Despite this, however, the predictions demonstrate the ability of LES to resolve the main characteristics of the turbulent flow while requiring a significantly less refined computational grid compared to DNS. In the context of the multiphase flows considered subsequently, this confirms the ability of LES to resolve those scales of turbulence that are mainly responsible of fluid-bubble interactions.

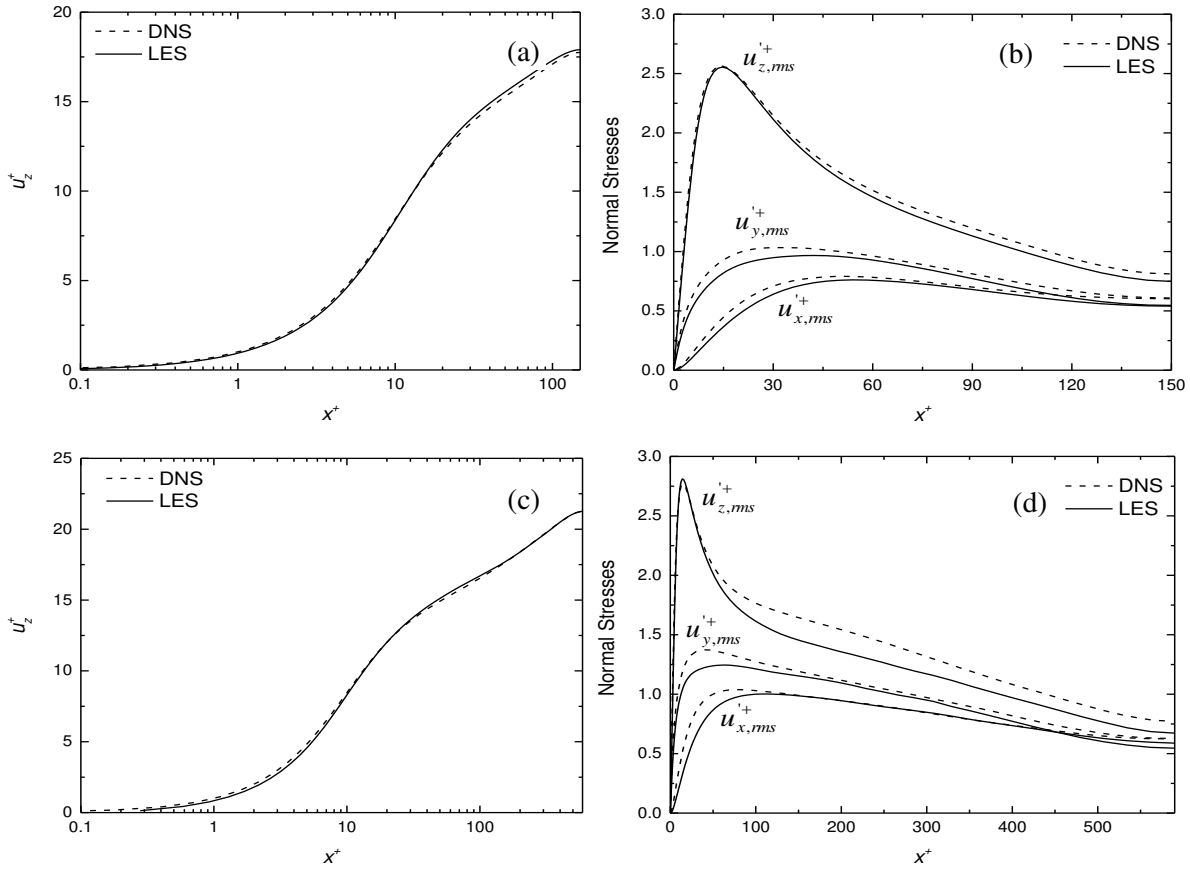

Figure 2: Single-phase velocity statistics: (a, c) mean streamwise velocity and (b, d) turbulent normal stresses for (a, b) $Re_\tau = 150$ and (c, d) $Re_\tau = 590$ flows.

Two-phase flow

The influence of bubbles on the continuous phase flow, and the bubble velocity and concentration fields, are investigated in this section. In Fig. 3, the mean fluid velocity profiles in the wall-normal direction are shown. More specifically, two-way coupled LES predictions are compared against the DNS of Molin et al.[15] at $Re_\tau = 150$ and for d_b = 110 μm and 220 μm in both upward and downward flow directions. To these predictions, the accuracy of which for

mean fluid and bubble velocity was previously demonstrated in Asiagbe et al.[31], additional LES-based results are added for d_b = 330 μm. In Fig. 4, the same profiles and comparisons are shown for the mean bubble streamwise velocity. Overall, the LES results for the mean fluid and bubble velocities are in good agreement with the DNS-based predictions, where available, for both the upflow and downflow cases. Moreover, the effect of the different flow configuration is clearly visible in each of the plots by comparison with the single-phase profile. More specifically, there is a distinct difference between the velocity profiles, with fluid and bubbles travelling faster in upflow and slower in downflow with respect to the single-phase flow. This difference, which follows from the boundary condition used where the total pressure loss across the channel was kept constant rather than using a fixed mass flow rate, is a function of the bubble diameter, with the difference increasing with bubble diameter for the bubble velocity, which becomes progressively higher in upflow and lower in downflow, whilst decreasing for the fluid velocity. This is due to the increase, with bubble diameter, of the role of the buoyancy force, which is proportional to bubble volume, with respect to the drag force, which is instead proportional to the bubble surface area. This means that the relative velocity between the bubbles and the fluid increases due to the increasing influence of buoyancy with bubble size, whereas the liquid mean velocity becomes more similar to that of the single-phase since the predicted drag from the bubbles, relative to the buoyancy force, reduces with their size.

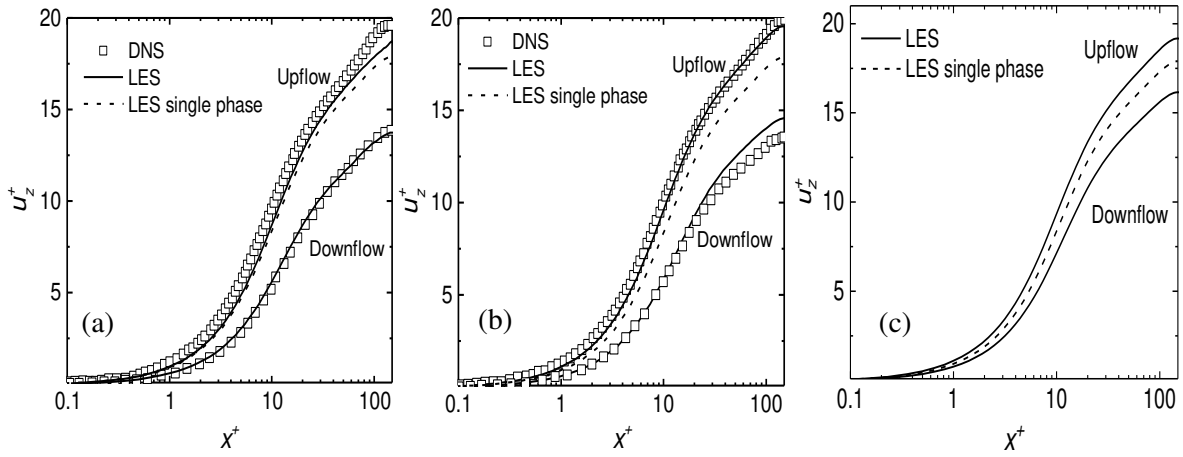

Figure 3: Bubble affected mean fluid streamwise velocity for the three bubble sizes at Reynolds number $Re_\tau = 150$: (a) d_b = 110 μm; (b) d_b = 220 μm; and (c) d_b = 330 μm.

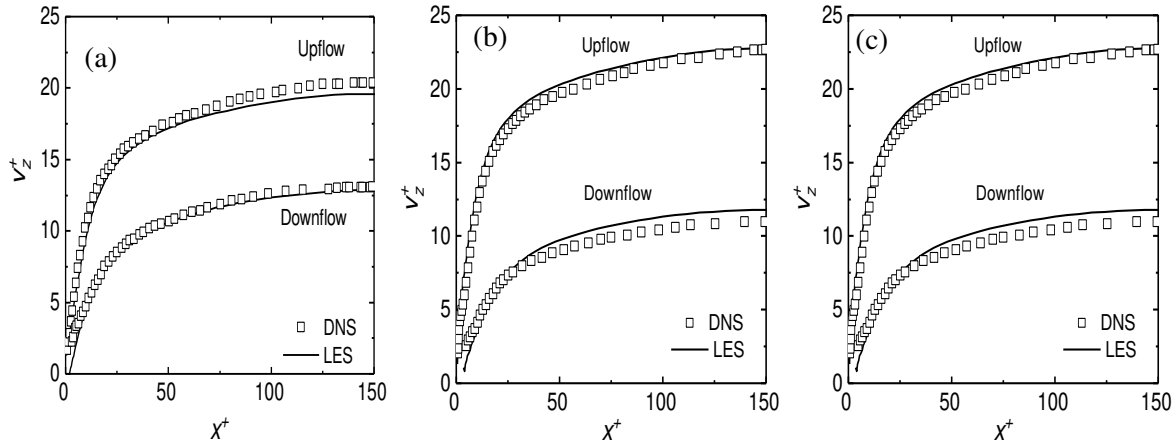

Figure 4: Mean bubble streamwise velocity for the three bubble sizes at Reynolds number $Re_\tau = 150$: (a) d_b = 110 μm; (b) d_b = 220 μm; and (c) d_b = 330 μm.

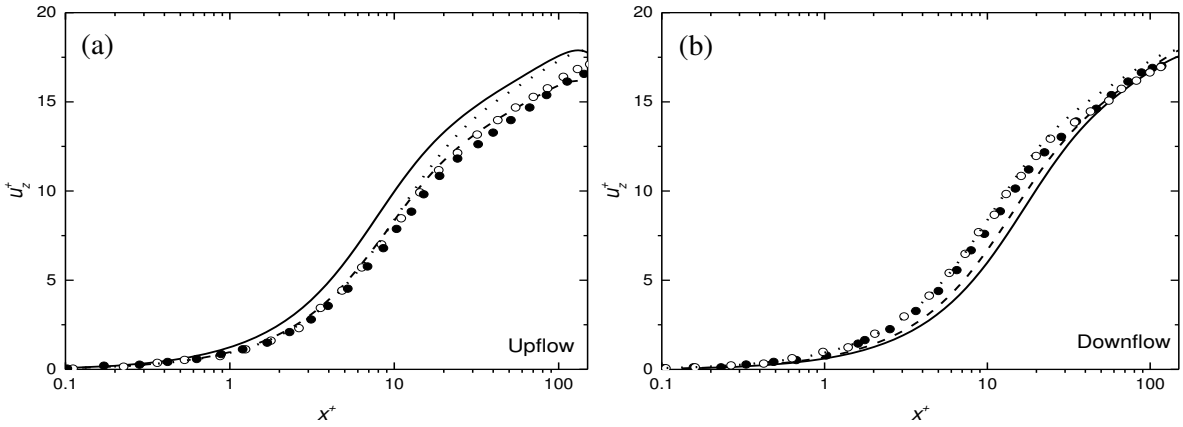

Figure 5: Mean fluid streamwise velocity rescaled with the effective shear velocities at Reynolds number $Re_\tau = 150$: (a) upflow; and (b) downflow (--- LES, $d_b = 110$ μm; — LES, $d_b = 220$ μm; • DNS, d_b = 110 μm; ○ DNS, $d_b = 220$ μm; ··· LES single-phase).

In Fig. 5, the mean fluid streamwise velocity for bubble sizes d_b = 110 and 220 μm is rescaled using the effective upflow and downflow shear velocities after the introduction of the bubbles, and compared against rescaled DNS-based predictions. As noted by Molin et al.[15], the difference that is observed in the results of Fig. 3 is reduced when the upflow and downflow shear velocities are used to scale the velocity profiles. More specifically, the LES profiles are almost superimposed and remain close to the single-phase profile in both flow configurations. As already noted, the total pressure drop is kept constant in these simulations, but the gravitational loss in upflow, and gain in downflow, is modified by the introduction of bubbles. Therefore, because of the reduced gravitational loss, the upflow is almost equal to a single-phase flow driven by an increased pressure gradient. In a similar way, the downflow is

equivalent to a flow driven by a reduced pressure gradient because of the reduced gravitational gain.

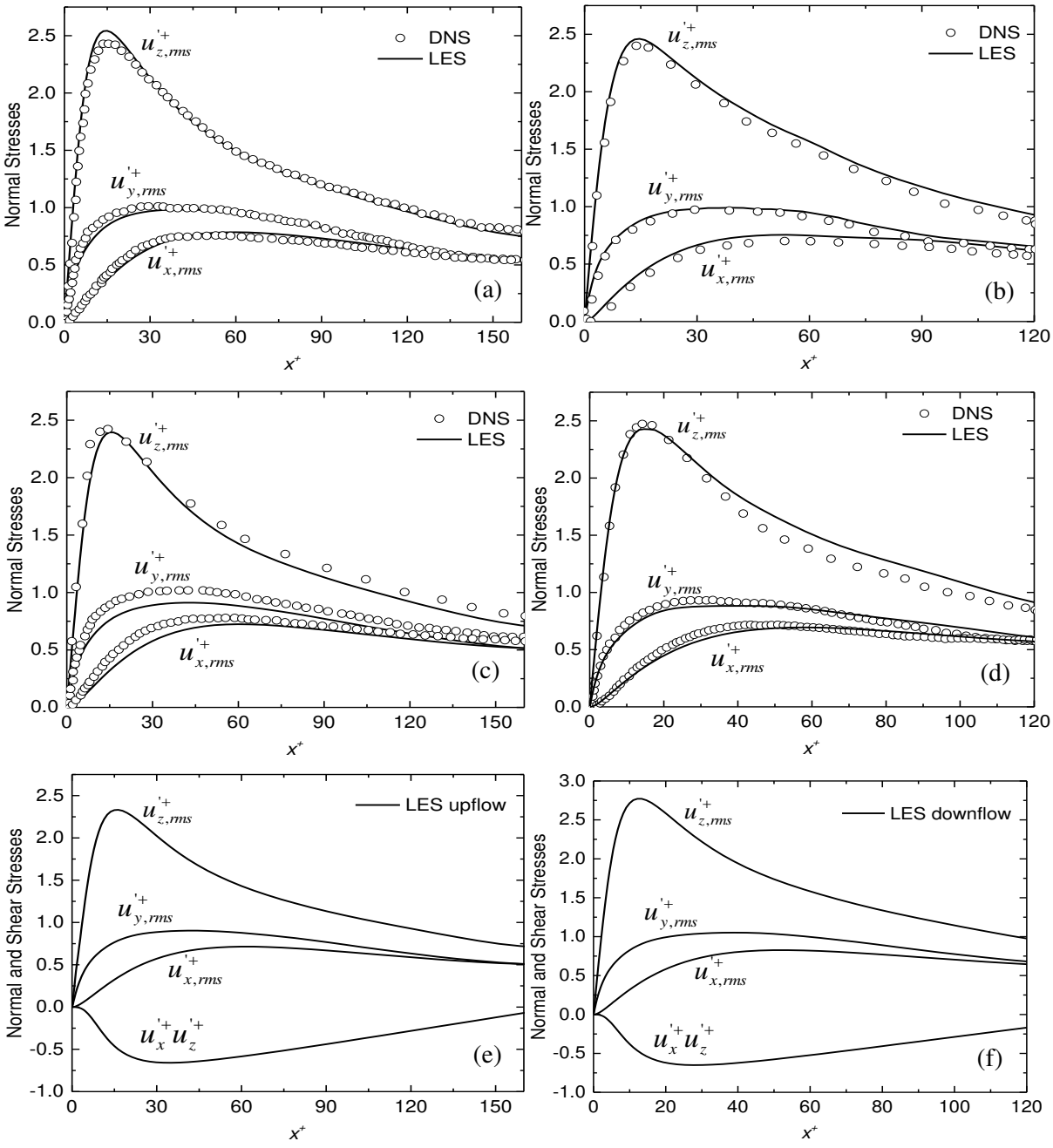

Figure 6: Fluid statistics scaled with effective upflow and downflow shear velocity compared with DNS data (where available) for (a, b) $d_b = 110$ µm, (c, d) $d_b = 220$ µm and (e, f) $d_b = 330$ µm. Upflow left hand and downflow right hand plots.

The r.m.s. of the fluid velocity fluctuations, scaled using the upflow and downflow shear velocities, are given in Fig. 6 for the three bubble sizes considered. Shear stresses are also given for the largest bubble case for which DNS predictions are not available, although for the 110

and 220 µm bubbles comparisons are made with the results of Molin et al.[15]. In both upflow and downflow, the bubbles alter not only the mean flow velocity, as noted above, but also the fluid turbulence, and this effect is well reproduced by the LES which shows good agreement with DNS-based predictions, where available. When scaled using the actual shear velocities, r.m.s. values in Fig. 6 look similar to those in the single-phase flow given in Fig. 2. Therefore, not only for the mean velocity, but also for the turbulence in the fluid, the upflow is equivalent to a single-phase flow with a slightly higher mass flow rate, and the downflow to a flow with a lower mass flow rate. Overall, an increase in flow rate results in corresponding increases of the turbulence in upflow (r.m.s. scaled using a higher shear velocity), whereas the reduction in downflow produces lower turbulence fluctuations. In addition, there is also an effect of the bubble diameter on the fluid turbulence since the largest deviations with respect to the single-phase flow are for the 330 µm case.

The r.m.s. of the velocity fluctuations of the bubbles is given in Fig. 7 for bubble sizes d_b = 110 and 220 µm, for which LES results are compared with those based on DNS from Molin et al.[15], and, for LES only, at d_b = 330 µm, in both upflow and downflow configurations. In these plots, r.m.s. values are scaled using the fluid-only, single-phase shear velocity. As is clearly shown, in upflow conditions the turbulent fluctuations are considerably higher than in the downflow case, and enhanced with respect to those of the continuous phase (Fig. 6). In contrast, in downflow the turbulence levels are decreased with respect to the single-phase fluid. These effects, noted in Molin et al.[15], are well-reproduced by the LES, with results in good agreement with the DNS-based solutions, and with similar trends found in the LES alone for a bubble diameter d_b = 330 µm. It should be noted that, in downflow, and in particular for bubble diameters of 220 and 330 µm, the turbulence profiles are not defined in the very near-wall region. This is due, as will be discussed in more detail below, to the small number of bubbles in this region due to bubble interaction with the fluid phase.

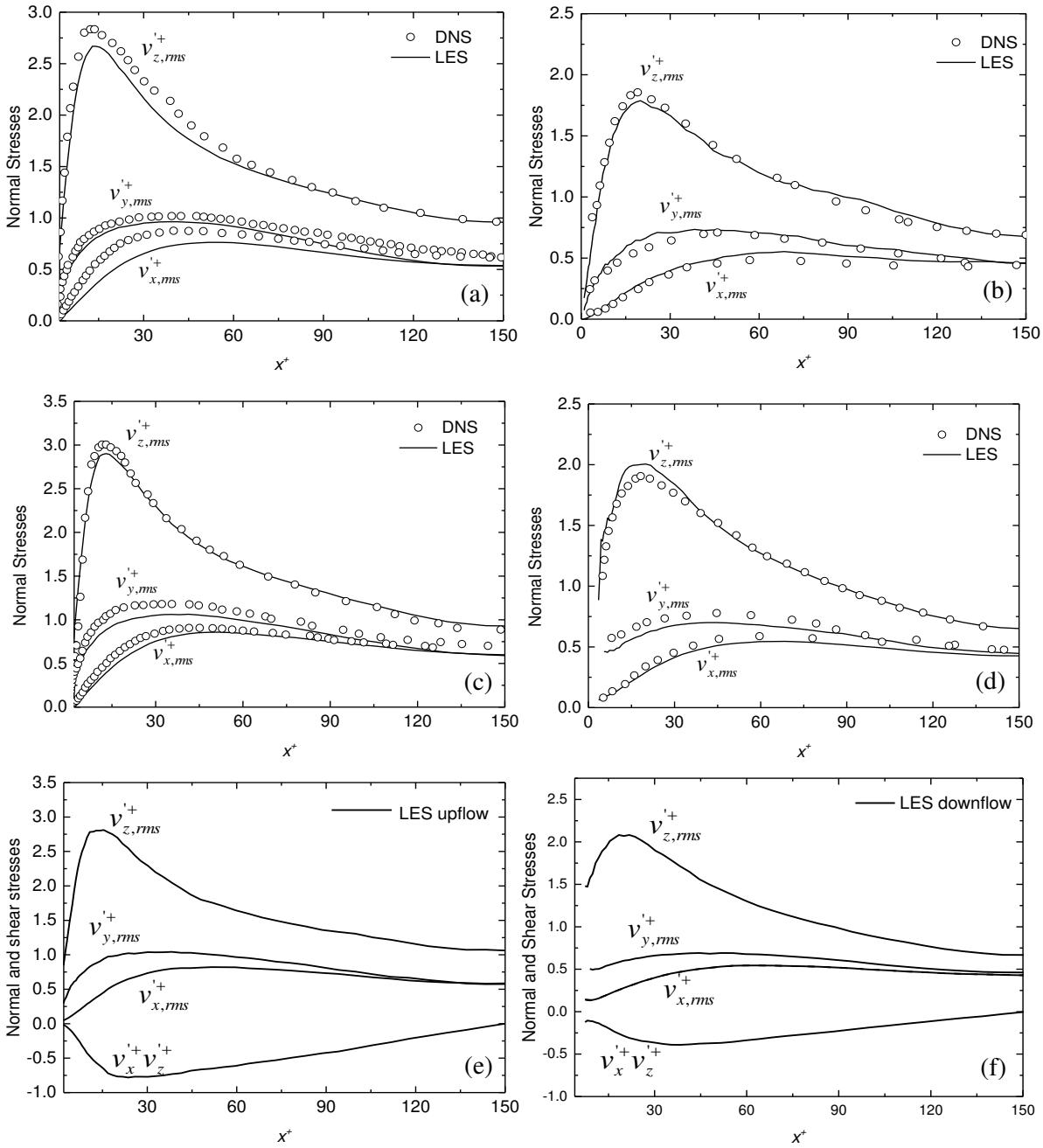

Figure 7: Bubble statistics scaled with single-phase shear velocity compared with DNS (where available) for (a, b) d_b = 110 μm, (c, d) d_b = 220 μm and (e, f) d_b = 330 μm. Upflow left hand and downflow right hand plots.

For microbubble flows, and for bubbly flows in general, of significant interest is how the distribution and concentration of the bubbles are affected by the fluid phase, and in particular by the levels of turbulence within the flow. As a consequence of their interaction with the continuous phase, bubbles may concentrate in specific regions of the flow and leave other areas depleted. In pipes and channels, it has been observed how small bubbles, that tend to remain spherical, concentrate near the wall in upflow and in the centre of the flow in downflow[9,14].

This effect has been generally attributed to the action of the lift force, which pushes the bubbles perpendicularly to the direction of the main fluid motion, and in the direction of the negative, in upflow, and positive, in downflow, fluid velocity gradient[31].

The time evolution of the bubble concentration in the wall-normal direction in both upflow and downflow is shown in Figs. 8 to 10 for the three bubble sizes considered. In these figures, both the full cross-channel profiles across the whole vertical channel width is shown, together with details in the wall region. To compute the bubble concentration, a number of divisions in the wall-normal direction was used, with the average number of bubbles within each region, n_b, determined and divided by the volume of that region, V, to obtain the local concentration $C = n_b/V$. The local concentration was then normalized by its initial value C_0. The ratio C/C_0 is therefore the normalized bubble number density which is greater than unity in flow regions were bubbles tend to segregate and smaller than unity in regions depleted of bubbles. The plots show concentration profiles averaged over the time intervals noted in the figures.

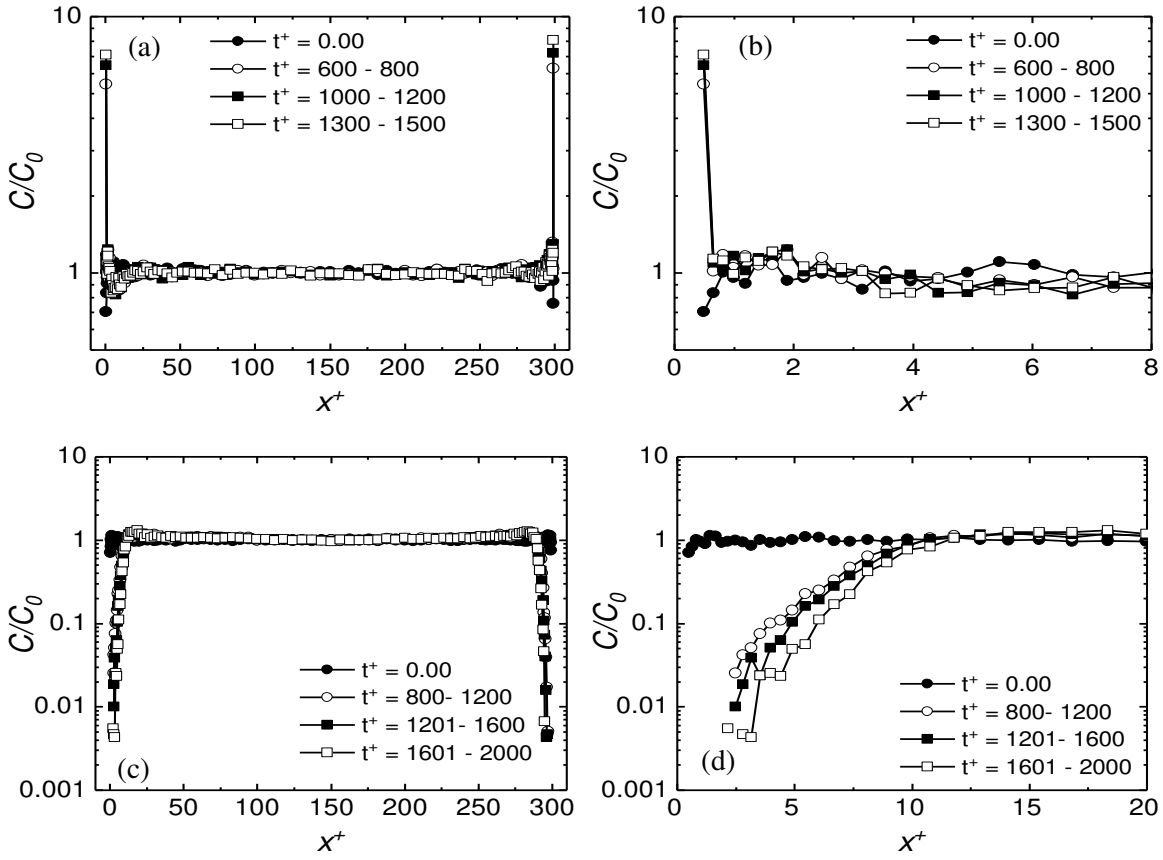

Figure 8: Time evolution of microbubble concentration in the wall-normal direction for shear Reynolds number $Re_\tau = 150$ and $d_b = 110$ μm. Upflow: (a) whole channel profile; (b) near-wall region. Downflow: (c) whole channel profile; (d) near-wall region.

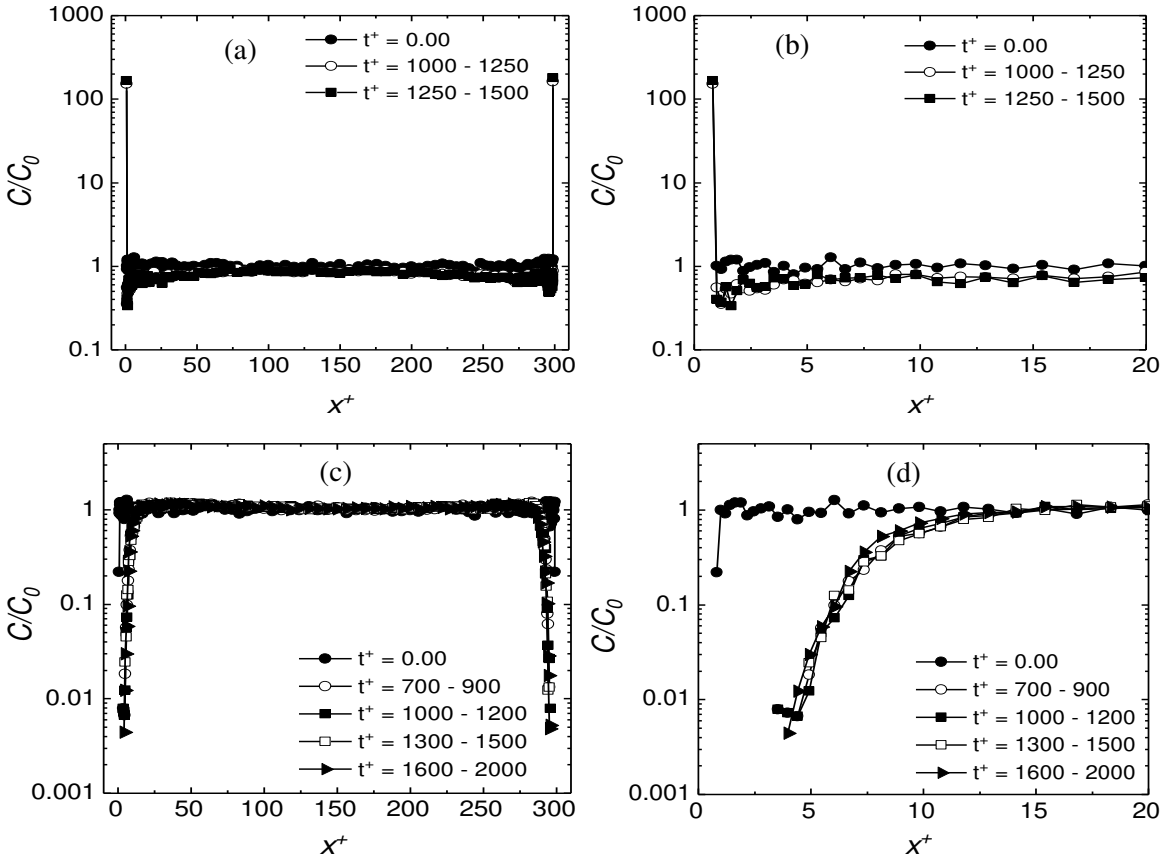

Figure 9: Time evolution of microbubble concentration in the wall-normal direction for shear Reynolds number $Re_\tau = 150$ and $d_b = 220$ µm. Upflow: (a) whole channel profile; (b) near-wall region. Downflow: (c) whole channel profile; (d) near-wall region.

The results show symmetric profiles of bubble concentration under all conditions. Starting from a uniform distribution at the beginning of a run, in upflow the bubbles tend to accumulate near the wall, generating a wall-peaked distribution. In contrast, in downflow the bubbles are moved from the near-wall region towards the channel centre resulting, ultimately, in very low concentrations of bubbles close to the wall[31]. These bubble-depleted regions near the walls are responsible for the problems noted above in relation to determining turbulent bubble statistics due to the small bubble sample size when averaging. The concentration profiles obtained confirm findings from previous studies[14,52,53]. Looking at the results in more detail, it is evident that the increase or decrease of bubble concentration near the wall, and the extent of the region affected (in particular for the downflow case), increases with bubble diameter. More specifically, the concentration in upflow increases from approximately 10 for d_b = 110 µm (Fig. 8b) to more than approximately 250 for d_b = 330 µm (Fig. 10). In downflow, the bubble-depleted region ends to $x^+ \approx 10$ in Fig. 8 and to about $x^+ = 20$ in Fig. 10, with the extent of

bubble depletion in these regions also increasing with bubble diameter. To investigate this phenomenon, and the resulting form of the concentration profiles obtained, the magnitude of the forces acting on the bubbles in the wall-normal direction is analysed in the following section.

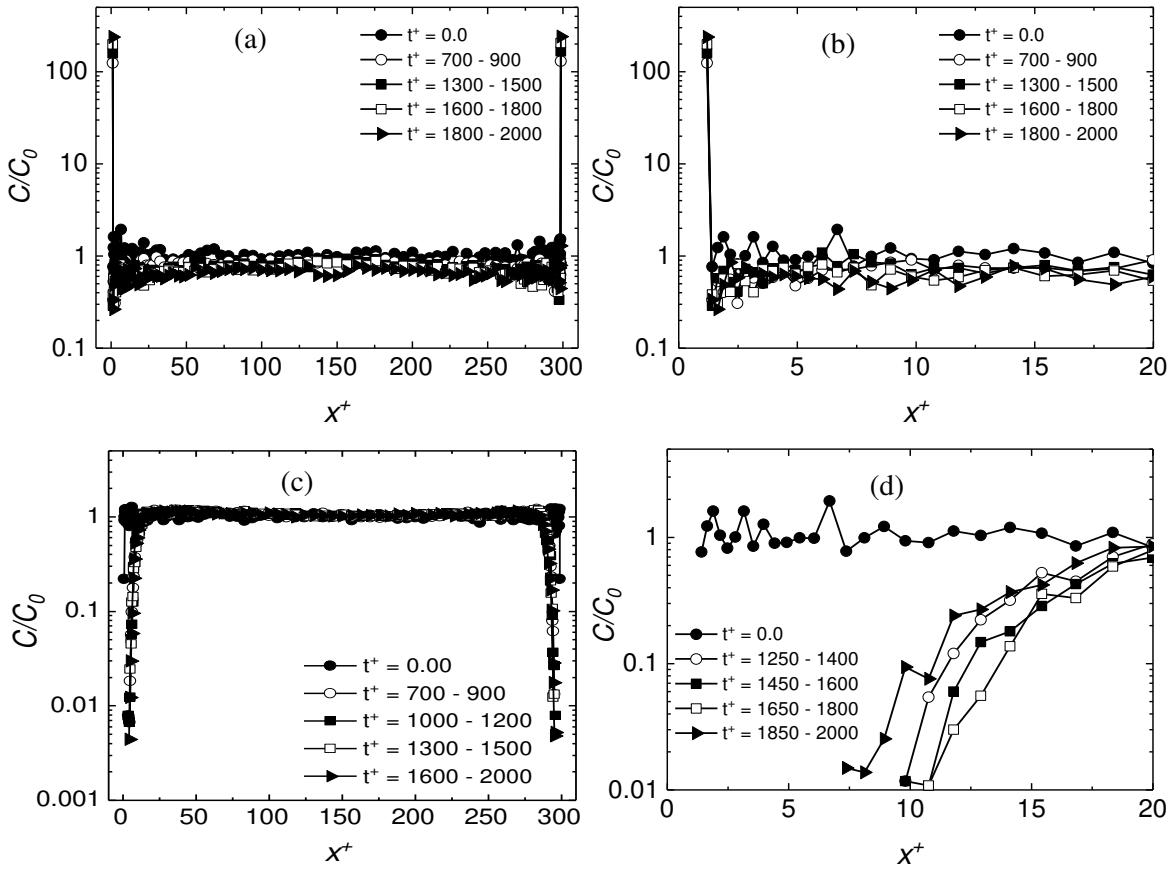

Figure 10: Time evolution of microbubble concentration in the wall-normal direction for shear Reynolds number $Re_\tau = 150$ and $d_b = 330$ µm. Upflow: (a) whole channel profile; (b) near-wall region. Downflow: (c) whole channel profile; (d) near-wall region.

Force analysis in the wall-normal direction

The forces acting on the bubbles (force per unit mass in N kg^{-1}) are shown for both upflow and downflow in Fig. 11, with results only given for the d_b = 220 µm case as the other bubble sizes showed similar trends. Overall, the drag and lift forces tend to be dominant, with the lift force pushing bubbles closer to the wall in upflow and towards the centre of the channel in downflow. This is confirmed by the change in sign in the lift force between the upflow to downflow cases. The lift force is also always opposed and balanced by the drag force[31]. Clearly, both gravity and buoyancy do not play a significant role in the wall-normal direction, with their effect acting

in the vertical direction. There is also a not insignificant effect of the added mass and pressure gradient forces, although they are an order of magnitude less than the lift and drag forces. Both of these forces are directed towards the centre of the flow near the wall and, to a lesser extend, towards the wall in the centre of the channel. Therefore, in the near-wall region, they oppose the lift force in upflow and, in contrast, they support the lift force in downflow.

The role of the lift force is also addressed in Fig. 12, where its magnitude for the three different bubble sizes is compared for the upflow and downflow cases. In both flow configurations, the magnitude of the lift force increases with bubble diameter, as would be anticipated. This is in agreement with earlier results (Figs. 8-10) where, in the wall region, the concentration peak near the wall in upflow, and the extent of the depleted region in downflow, were found to increase with the bubble diameter.

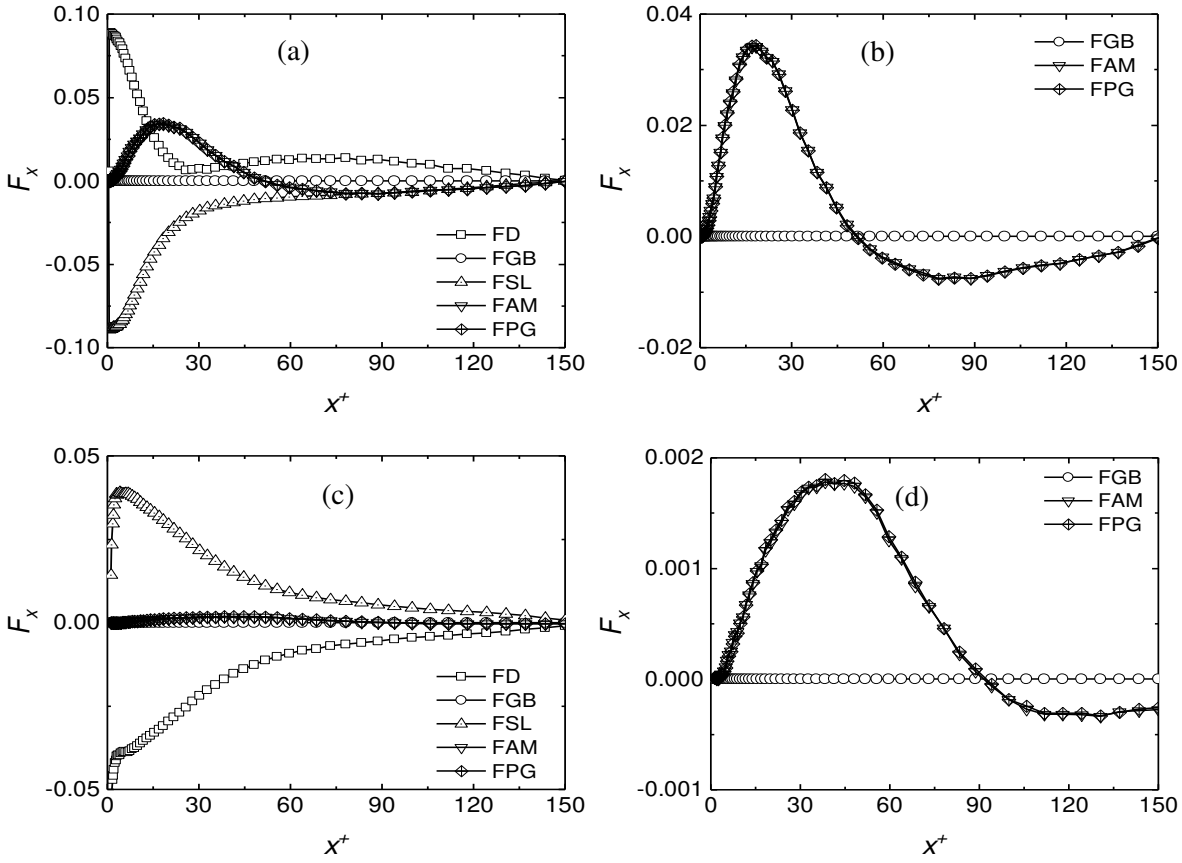

Figure 11: Forces acting in the wall-normal direction on d_b = 220 μm bubbles for Re_τ = 150: (a, b) upflow; (c, d) downflow. Plots (b) and (d) show an expanded ordinate scale to show relative magnitude of smaller forces (FD = drag force, FGB = gravity-buoyancy force, FSL = shear lift force, FAM = added mass force, FPG = pressure gradient force).

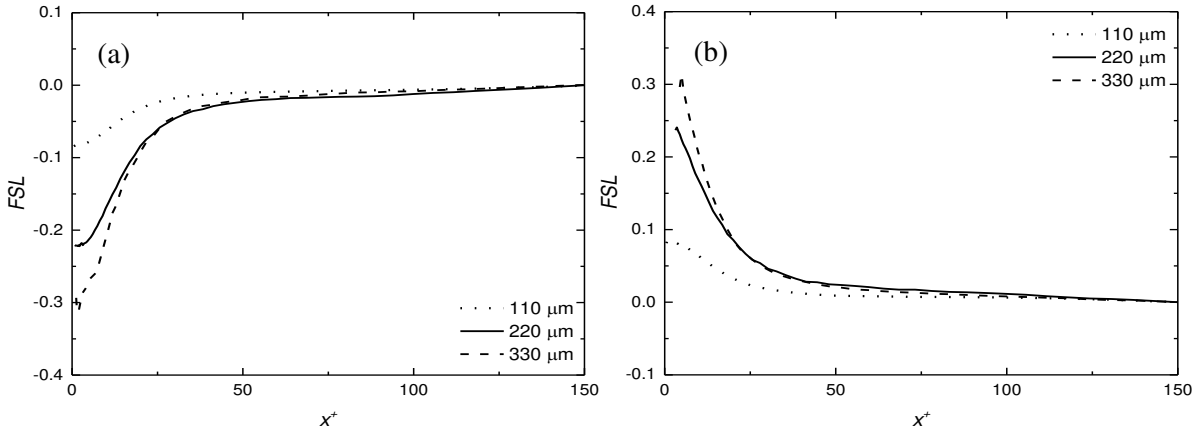

Figure 12: Wall-normal component of the lift force acting on different sizes of bubble; (a) upflow; and (b) downflow.

Effect of Reynolds number

Since turbulence can significantly affect bubble behaviour, additional simulations were also performed at $Re_\tau = 590$ to study its effect on microbubble dispersion in vertical channels, taking advantage of the less-demanding computational resources required by LES when compared to DNS. For these simulations, a single bubble diameter of 220 μm was used. Figure 13 shows fluid and bubble mean velocity and turbulence statistics for both upflow and downflow cases[31], with bubble concentration profiles and the forces acting on the bubbles in the wall-normal direction presented in Figs. 14 and 15, respectively. The distinctive differences between upflow and downflow, which were apparent at a shear Reynolds number $Re_\tau = 150$, are greatly reduced at $Re_\tau = 590$, with both mean fluid velocity profiles peaking at around 22.5 in the centre of the channel. There is also little variation in the fluid turbulent statistics between the two cases, with the normal and shear stress profiles closer to the corresponding single-phase as a result of the higher turbulence levels that dominate the influence of the bubbles on the continuous phase. Mean bubble velocities in the two flow directions also show significantly reduced differences with respect to the same bubble diameter at shear Reynolds 150, with the upflow peaking at approximately 22.5 and the downflow at 20.5. The relative velocity between the fluid and the bubbles is mostly a function of the bubble diameter, therefore it does not change significantly with an increase in the fluid velocity. Instead, the velocity magnitude and turbulence statistics of both the fluid and the bubbles are greatly increased at the higher shear Reynolds number. Therefore, the ratio of the relative velocity to the velocity

magnitude is significantly reduced, and hence the magnitude of the differences between the upflow and downflow profiles is likewise decreased.

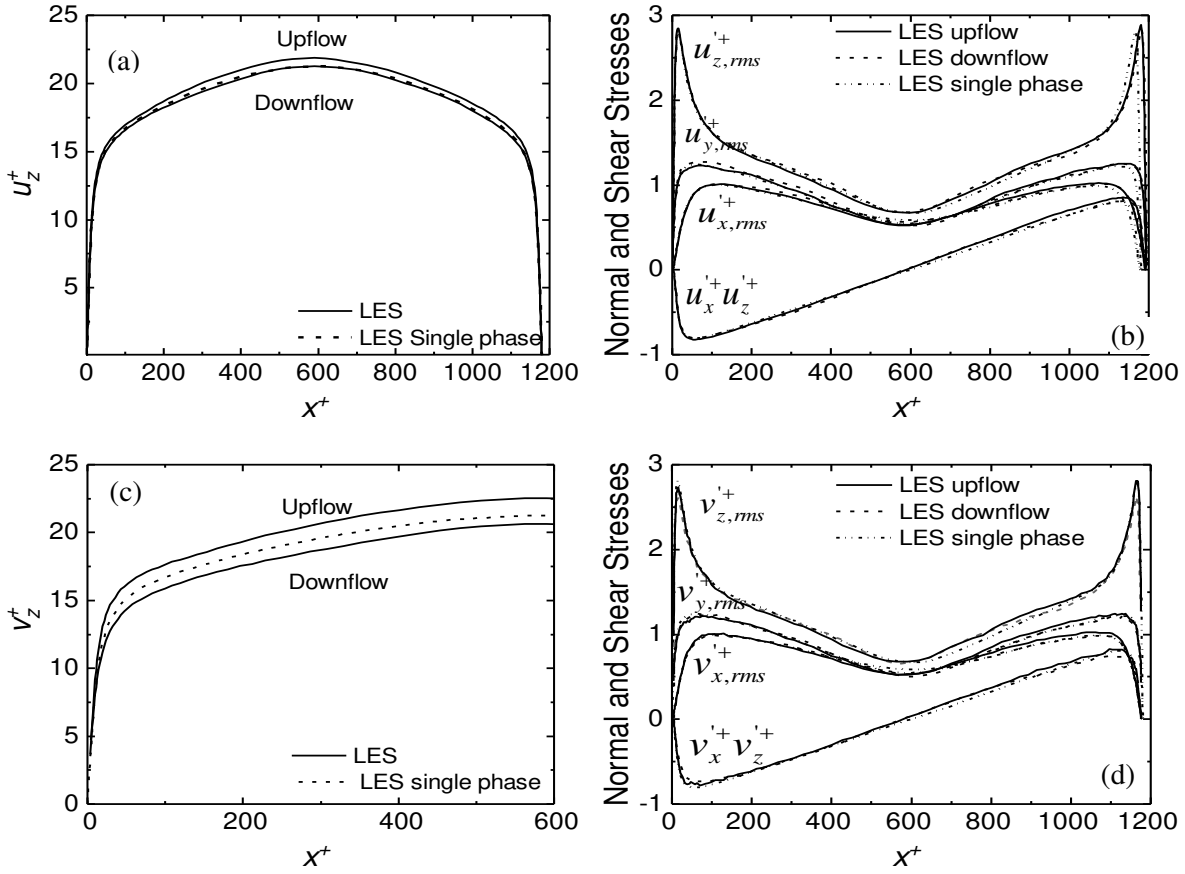

Figure 13: Fluid and bubble statistics for Re_τ = 590 and $d_b = 220\ \mu m$, in comparison with single-phase: (a) bubble affected mean fluid streamwise velocity; (b) bubble affected fluid normal and shear stresses; (c) mean bubble streamwise velocity; and (d) bubble normal and shear stresses.

Figure 14 shows the time evolution of microbubble concentration in the wall-normal direction. The distribution profiles show a similar pattern to those of the Re_τ = 150 flow, with bubbles concentrating near the wall in upflow and moving towards the channel centre in downflow. However, the peak value of the bubble concentration in upflow, and to a much lesser extent the width and magnitude of the bubble depleted region in downflow, are both reduced because of the increased dispersion of the microbubbles due to the higher turbulence levels. To better illustrate this, concentration profiles for a bubble size of $d_b = 220$ μm at $t^+ = 1500$ are compared for both upflow and downflow conditions in Fig. 14(e, f). This confirms that higher

levels of the turbulence enhance bubble mixing, generating more homogeneous concentration profiles and partially overwriting the effect of other forces.

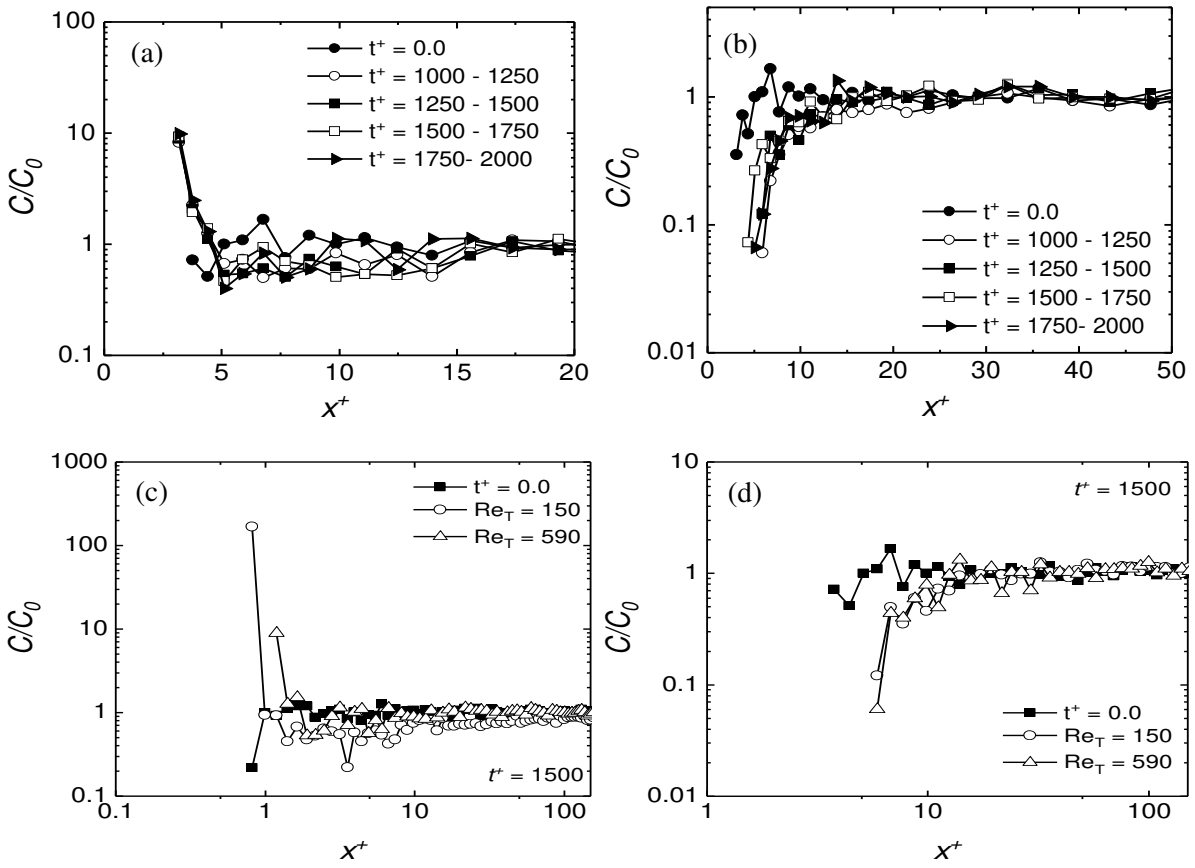

Figure 14: Time evolution of microbubble concentration in the wall-normal directions for shear Reynolds number $Re_\tau = 590$ and $d_b = 220\,\mu m$: a, upflow; b, downflow; and (c, d) concentration profiles for two reference Reynolds numbers for upflow and downflow, respectively at $t^+ = 1500$.

The forces acting on the bubbles are given for the Re_τ = 590 flow in Fig. 15. The lift force, which was dominant at $Re_\tau = 150$, is now slightly more confined to the near-wall region for both upflow and downflow cases, although of a higher magnitude. In contrast, in the remaining regions of the channel, the pressure gradient and added mass forces, which are more related to the fluid and bubble velocity magnitude, are now significant. The effect of the high turbulence levels is therefore to partially override the forces acting on the bubbles, with their behaviour now more in line with that of the fluid. Since increases in turbulence lead to increases in the vorticity of the flow, the added mass and pressure gradient forces, which are hydrodynamic forces, consequently increase in magnitude in those regions where the vorticity is high. An intermediate Reynolds number simulation at $Re_\tau = 300$ with the same bubble size, not shown

here, gave pressure gradient and added mass forces of a magnitude intermediate between those observed for the $Re_\tau = 150$ and 590 cases. The forces analysis plots in Fig. 15 agree qualitatively with those of Spelt and Sangani[54] who demonstrated that at high Reynolds number the liquid phase pressure force increases from zero, attains a maximum value, and subsequently decreases with distance from the wall. To balance these effects, the drag force changes sign in the upflow case, with respect to the $Re_\tau = 150$ case, apart from very close to the wall where it acts against the lift force, whilst it remains acting in opposition to the lift force at all locations in downflow.

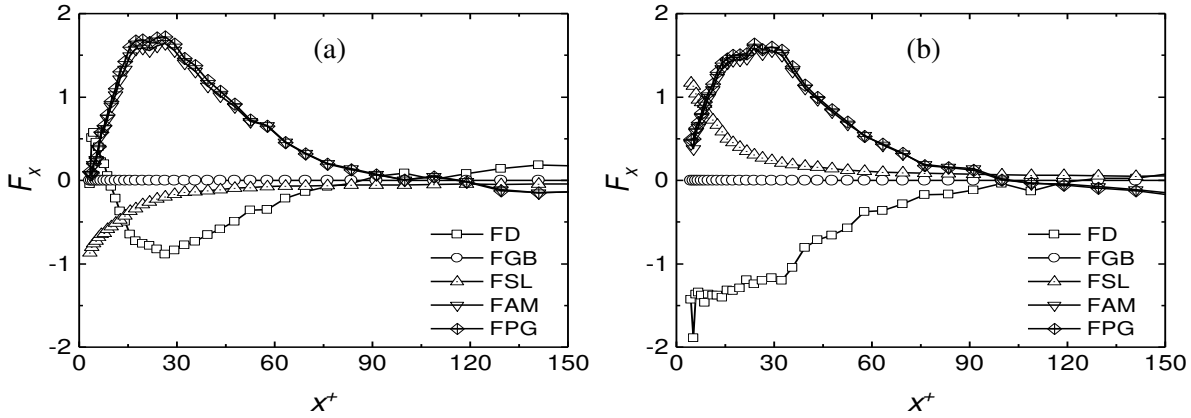

Figure 15: Forces acting in the wall-normal direction on d_b = 220 μm bubbles for $Re_\tau = 590$: (a) upflow; and (b) downflow (FD = drag force, FGB = gravity-buoyancy force, FSL = shear lift force, FAM = added mass force, FPG = pressure gradient force).

Conclusions

In the work described, the behaviour of microbubbles in a vertical turbulent channel flow of water was investigated using LES coupled with a Lagrangian bubble tracking routine. Both upflow and downflow configurations were simulated, and the effect on the fluid of the bubbles was accounted for through a two-way coupled approach. The model was first successfully validated against single-phase results, and DNS-based results[15] for two-phase flows at Re_τ = 150 and with bubble diameters of 110 and 220 μm. At Re_τ = 150, simulations at a bubble diameter of 330 μm were also carried out. This extends the range of bubble diameters previously considered in the literature and allowed the generation of additional understanding on the role of the bubble size on the coupled interactions between the bubble and the fluid, and fluid-driven bubble preferential concentration. Overall, the presence of the microbubbles strongly influences the fluid flow which becomes similar to a single-phase fluid flow at a higher mass flow rate in upflow and at a lower mass flow rate in downflow. Fluid turbulence is

enhanced in upflow and reduced in downflow, and the velocity fluctuations of the bubbles are higher in upflow and lower in downflow with respect to the fluid phase. A different bubble distribution is found in the two flow configurations, with bubbles segregating at the wall in upflow and moving towards the centre of the channel in downflow. In the wall-normal direction, the lift force is dominant at a shear Reynolds number of 150 and is largely responsible for the observed bubble distributions.

The use of LES also allowed the simulation of a higher shear Reynolds number flow, with Re_τ = 590, considerably higher than comparable DNS-based studies available in the literature. The increased turbulence dispersion at this Reynolds number reduced the peak value of the bubble concentration in upflow, and to a lesser extent the width and magnitude of the bubble depleted region in downflow. The lift force remained dominant only in regions very close to the wall. In the remainder of the channel, however, the pressure gradient and the added mass forces become more influential.

Overall, the LES-based results provide insight into the mechanisms of interfacial momentum transfer and turbulence modulation, and support the development of improved closures in macroscopic averaged models. With respect to DNS, the less demanding computational requirements of LES promises to enable the prediction of bubbly flows at Reynolds numbers of industrial and engineering interest. At the same time, the accuracy obtained suggests that the level of detail obtained from this technique is sufficient to describe the fluid structures that affect bubble behaviour, as well as the influence of bubbles on the continuous flow. In this context, the present model will be used in future as a starting point for further investigations of practically-relevant flows by extending the physical description to accommodate four-way coupling able to account for bubble collisions, coalescence and break-up.

Acknowledgements

KSA gratefully acknowledges the financial support of the Niger Delta Development Commission in Nigeria, and the opportunities that funding has given him.

References

1. Ekambara K, Sanders RS, Nandakumar K, Masliyah JH. CFD Modeling of Gas-Liquid Bubbly Flow in Horizontal Pipes: Influence of Bubble Coalescence and Breakup. International Journal of Chemical Engineering. 2012;2012:20.
2. Poullikkas A. Effects of two-phase liquid-gas flow on the performance of nuclear reactor cooling pumps. Progress in Nuclear Energy. 2003;42(1):3-10.

3. Bernal JAJ. Microbubble Drag Reduction Phenomenon Study in a Channel Flow. Texas A&M University. 2004.
4. Bunner B, Tryggvason G. Effect of bubble deformation on the properties of bubbly flows. Journal of Fluid Mechanics. 2003;495:77-118.
5. Esmaeeli A, Tryggvason G. Direct numerical simulations of bubbly flows. Part 1. Low Reynolds number arrays. Journal of Fluid Mechanics. 1998;377:313-345.
6. Abdulmouti H, Bubbly Two-Phase Flow: Part II- Characteristics and Parameters. American Journal of Fluid Dynamics. 2014;4(4):115-180.
7. James BL. Pressure and Diffusion Driven Bubble Growth on a Static Surface: Aerospace and Mechanical Engineering. University of Notre Dame. 2006.
8. Elghobashi S. On predicting particle-laden turbulent flows. Applied Scientific Research. 1994;52(4):309-329.
9. Wang LP, Maxey MR. Settling velocity and concentration distribution of heavy particles in homogeneous isotropic turbulence. Journal of Fluid Mechanics. 1993;256:27-68.
10. Tomiyama A, Tamai H, Zun I, Hosokawa S. Transverse migration of single bubbles in simple shear flows. Chemical Engineering Science. 2002;57(11):1849-1858.
11. Lucas D, Tomiyama A. On the role of the lateral lift force in poly-dispersed bubbly flows. International Journal of Multiphase Flow. 2011;37(9):1178-1190.
12. Colombo M, Fairweather M. Multiphase turbulence in bubbly flows: RANS simulations. International Journal of Multiphase Flow. 2015;77:222-243.
13. Colombo M, Fairweather M. Accuracy of Eulerian–Eulerian, two-fluid CFD boiling models of subcooled boiling flows. International Journal of Heat and Mass Transfer. 2016;103:28-44.
14. Giusti A, Lucci F, Soldati A. Influence of the lift force in direct numerical simulation of upward/downward turbulent channel flow laden with surfactant contaminated microbubbles. Chemical Engineering Science. 2005;60(22):6176-6187.
15. Molin D, Marchioli C, Soldati A. Turbulence modulation and microbubble dynamics in vertical channel flow. International Journal of Multiphase Flow. 2012;42(0):80-95.
16. Asiagbe KS, Fairweather M, Njobuenwu DO, Colombo M. Large eddy simulation of microbubble transport in a turbulent horizontal channel flow. International Journal of Multiphase Flow. 2017;94:80-93.
17. Schwarz S, Kempe T, Fröhlich J. An immersed boundary method for the simulation of bubbles with varying shape. Journal of Computational Physics. 2016;315:124-149.

18. Pakhomov MA, Terekhov VI. Application of the Eulerian approach to simulating the structure of an upward monodisperse bubbly flow in a tube. Journal of Applied Mechanics and Technical Physics. 2016;57(3):432-440.
19. Chahed J, Roig V, Masbernat L. Eulerian–Eulerian two-fluid model for turbulent gas–liquid bubbly flows. International Journal of Multiphase Flow. 2003;29(1):23-49.
20. Njobuenwu DO, Fairweather M, Yao J. Coupled RANS–LPT modelling of dilute, particle-laden flow in a duct with a 90° bend. International Journal of Multiphase Flow. 2013;50(0):71-88.
21. Pang M, Wei J, Yu B. Numerical study of bubbly upflows in a vertical channel using the Euler–Lagrange two-way model. Chemical Engineering Science. 2010;65(23):6215-6228.
22. Lau YM, Bai W, Deen NG, Kuipers JAM. Numerical study of bubble break-up in bubbly flows using a deterministic Euler–Lagrange framework. Chemical Engineering Science 2014;108(0):9-22.
23. Hosokawa S, Suzuki T, Tomiyama A. Effects of bubbles on turbulence properties in a duct flow. Multiphase Science and Technology. 2010;22(3):211-232.
24. Ervin EA, Tryggvason G. The rise of bubbles in a vertical shear flow. Journal of Fluids Engineering. 1997;119(2):443-449.
25. Pang M, Wei J, Yu B. Investigation on Influences of Bubble Location and Momentum Transfer Direction on Liquid Turbulence Modification for the Dilute Bubbly Flow. International Journal of Fluid Mechanics Research. 2016;43(2):161-181.
26. Pang M, Wei J, Yu B. Turbulence Modulation by Small Bubbles in the Vertical Upward Channel Flow. Advances in Mechanical Engineering. 2013;5:379839.
27. Delnoij E, Lammers FA, Kuipers JAM, Van Swaaij WPM. Dynamic simulation of dispersed gas-liquid two-phase flow using a discrete bubble model. Chemical Engineering Science. 1997;52:1429-1458.
28. Lain S, Bröder D, Sommerfeld M. Experimental and numerical studies of the hydrodynamics in a bubble column. Chemical Engineering Science. 1999;54(21):4913-4920.
29. Santarelli C, Fröhlich J. Direct Numerical Simulations of spherical bubbles in vertical turbulent channel flow. Influence of bubble size and bidispersity. International Journal of Multiphase Flow. 2016;81:27-45.

30. Asiagbe KS, Fairweather M, Njobuenwu DO, Colombo M. Multiscale Simulation of Bubbly Flows. In: Zdravko K, Miloš B. Computer Aided Chemical Engineering. 2016;38:625-630.
31. Asiagbe KS, Fairweather M, Njobuenwu DO, Colombo M. Large eddy simulation of microbubble transport in vertical channel flows. In: Espuna A., Graells M., Puigjaner L. Computer Aided Chemical Engineering. 2017;40:73-78.
32. Yamamoto Y, Potthoff M, Tanaka T, Kajishima T, Tsuji Y. Large-eddy simulation of turbulent gas–particle flow in a vertical channel: effect of considering inter-particle collisions. Journal of Fluid Mechanics. 2001;442:303-334.
33. Germano M, Piomelli U, Moin P, Cabot WH. A dynamic subgrid-scale eddy viscosity model. Physics of Fluids. 1991;3(7):1760-1765.
34. Piomelli U, Liu J. Large-eddy simulation of rotating channel flows using a localized dynamic model. Physics of Fluids. 1995;7(4):839-848.
35. di Mare L, Jones WP. LES of turbulent flow past a swept fence. International Journal of Heat and Fluid Flow. 2003;24(4):606-615.
36. Porté-Agel F, Meneveau C, Parlange MB. A scale-dependent dynamic model for large-eddy simulation: application to a neutral atmospheric boundary layer. Journal of Fluid Mechanics. 2000;415:261-284.
37. Lilly DK. The representation of small scale turbulence in numerical simulation experiments. Proceedings of the IBM Scientific Computing Symposium on Environmental Sciences, Yorktown Heights, USA, 1967.
38. Maxey MR, Riley JJ. Equation of motion for a small rigid sphere in a nonuniform flow. Physics of Fluids. 1983;26(4):883-889.
39. Rivero M, Magnaudet J, Fabre J. New results on the forces exerted on a spherical body by an accelerated flow. Comptes rendus de L'Academie des sciences Serie II. 1991;312:1499-1506.
40. Sridhar G, Katz J. Effect of entrained bubbles on the structure of vortex rings. Journal of Fluid Mechanics. 1999;397:171-202.
41. Schiller L, Naumann Z. A drag coefficient correlation. Ver. Deutsch. Ing. 1935;77:318.
42. Legendre D, Magnaudet J. A note on the lift force on a spherical bubble or drop in a low-Reynolds-number shear flow. Physics of Fluids. 1997;9(11):3572-3574.
43. Bini M, Jones WP. Large-eddy simulation of particle-laden turbulent flows. Journal of Fluid Mechanics. 2008;614:207-252.

44. Elghobashi S, Truesdell GC. Direct simulation of particle dispersion in a decaying isotropic turbulence. Journal of Fluid Mechanics. 1992;242:655-700.
45. Gamet L, Ducros F, Nicoud F, Poinsot T. Compact finite difference schemes on non-uniform meshes. Application to direct numerical simulations of compressible flows. International Journal for Numerical Methods in Fluids. 1999;29(2):159-191.
46. Shen WZ, Michelsen J, Sørensen JN. An improved Rhie-Chow interpolation for unsteady flow computations. AIAA Journal. 2001;39(12):2406-2409.
47. Jones WP, Marquis AJ, Vogiatzaki K. Large-eddy simulation of spray combustion in a gas turbine combustor. Combustion and Flame. 2014;161(1):222-239.
48. di Mare F, Jones WP, Menzies KR. Large eddy simulation of a model gas turbine combustor. Combustion and Flame. 2004;137(3):278-294.
49. Njobuenwu DO, Fairweather M. Dynamics of single, non-spherical ellipsoidal particles in a turbulent channel flow. Chemical Engineering Science. 2015;123(0):265-282.
50. Marchioli C, Soldati A, Kuerten JGM, Arcen B, Taniere A, Goldensoph G., Squires KD, Cargnelutti, MF, Portela LM. Statistics of particle dispersion in direct numerical simulations of wall-bounded turbulence: Results of an international collaborative benchmark test. International Journal of Multiphase Flow. 2008;34(9):879-893.
51. Moser RD, Kim J, Mansour NN. Direct numerical simulation of turbulent channel flow up to Reτ=590. Physics of Fluids. 1999;11(4):943-945.
52. Shams E, Finn J, Apte SV. A numerical scheme for Euler–Lagrange simulation of bubbly flows in complex systems. International Journal for Numerical Methods in Fluids. 2011;67(12):1865-1898.
53. Serizawa A, Kataoka I, Michiyoshi I. Turbulence structure of air-water bubbly flow—II. local properties. International Journal of Multiphase Flow. 1975;2(3):235-246.
54. Spelt PDM, Sangani AS. Properties and Averaged Equations for Flows of Bubbly Liquids. Applied Scientific Research. 1997;58(1):337-386.